Jahn-Teller transition of Fe_2TiO_4 observed by maximum entropy method at high pressure and low temperature

Takamitsu Yamanaka,[1,2,3] Tetsuro Mine,[2] Sachiko Asogawa,[2] and Yuki Nakamoto[3]
[1]*Geophysical Laboratory, Carnegie Institution of Washington, 5251 Broad Branch Road NW, Washington, DC 20015-1305, USA*
[2]*Department of Earth and Space Science, Osaka University, Machikaneyama, Toyonaka, Osaka 560-0043, Japan*
[3]*Center for Quantum Science and Technology under Extreme Conditions, Osaka University, Toyonaka, Osaka 560-0043, Japan*
(Received 9 May 2009; revised manuscript received 13 August 2009; published 22 October 2009)

Jahn-Teller transition of ulvöspinel Fe_2TiO_4 has been investigated by single-crystal x-ray diffraction study under high pressures up to 15 GPa at ambient temperature using synchrotron radiation and under the low-temperature condition down to −170 °C at ambient pressure. The transition from cubic to tetragonal is induced from the tetragonal distortion due to the Jahn-Teller effect of Fe^{2+} at the tetrahedral site. The phase transition takes place at 9 GPa with increasing pressure at 20 °C and the transition was found at −110 °C and 1 atm. The c/a ratio is 0.9982(4) at 11.43 GPa. On the other hand, the value is 1.0035(5) at −170 °C and 1 atm. Degeneracy of e orbit of $^{IV}Fe^{2+}$ is different between high-pressure and low-temperature conditions: the former prefers electronic state $d_{x^2-y^2}$ and the latter d_{z^2} orbit in e orbit. Difference Fourier maps on (100) and (001) planes of Fe_2TiO_4 reveal the electron density of e electrons of $^{IV}Fe^{2+}$. Orthorhombic structure of Fe_2TiO_4 at 30 GPa determined by Rietveld method was $CaTi_2O_4$-type structure by powder-diffraction study. In addition, we found another new higher-pressure polymorph at 48 GPa.

DOI: 10.1103/PhysRevB.80.134120 PACS number(s): 64.60.−i, 71.20.−b, 74.62.Fj, 61.50.Ks

I. INTRODUCTION

High-pressure phase transition of many spinels has attracted much attention from geophysical interests and industrial use, such as ferrites and semiconductors. Some spinels of $A^{2+}{}_2B^{4+}O_4$ (A=Mg,Fe,Co,Zn and B=Si,Ge,Ti) decompose directly or indirectly to ilmenite+B1, rutile+B1, and perovskite+B1 with increasing pressure. But some other spinels transform directly to the high-pressure postspinel phases without decomposition. The postspinel phases are $CaTi_2O_4$ (*Cmcm*), $CaMn_2O_4$ (*Pbcm*), and $CaFe_2O_4$ (*Pnma*) type structures.[1] Spinels with transition elements undergo their structure transitions with electron-lattice interactions under high pressures and low temperatures. High-pressure studies of spinels are paid a large attention in order to understand electronic strong correlation such as the charge transfer, electron hopping, electron high-low spin transition, Jahn-Teller distortion, and charge disproponation.

Tetragonal spinels induced from Jahn-Teller distortion by $^{IV}Fe^{2+}$, $^{IV}Cu^{2+}$, $^{VI}V^{3+}$, $^{VI}Mn^{3+}$, and $^{VI}Ti^{3+}$ are listed in Table I. Among these spinels, tetragonal spinel induced by tetrahedral cations are very rare, such as Fe_2TiO_4,[2] $CuFe_2O_4$,[3,4] $MgTi_2O_4$,[5,6] $CuCr_2O_4$,[7] and $CuRh_2O_4$.[7] It has been reported that Fe_2TiO_4 transforms from cubic ($Fd3m$) to tetragonal ($I4_1/amd$) phase below −110 °C by magnetostriction measurement together with powder diffraction (Ishikawa and Syono, 1971).[2]

From geophysical interest of rock magnetism, cation distributions of titanomagnetite solid solution $Fe_{3-x}Ti_xO_4$ have been investigated by x-ray diffraction, neutron diffraction, magnetic measurement, and Mössbauer experiments.[8–14] Diamond-anvil cell (DAC) and synchrotron-radiation (SR) facilities enable us to elucidate the structures of high-pressure polymorphs. Powder diffraction experiment up to 60 GPa (Ref. 1) has been executed to clarify the phase relations of high-pressure polymorphs using SR. $Fe_{3-x}Ti_xO_4$, solid solutions have an inverse spinel structure in the whole compositional range. The observed lattice constants, oxygen positional parameter, and the volumes of the tetrahedral and octahedral sites support the model in which Ti always prefers the octahedral site. The transition from cubic spinel to orthorhombic structure of $CaTi_2O_4$ (*Cmcm*) is confirmed in the whole compositional range and the transition pressure decreases from 27 GPa (x=0.0) to 11 GPa (x=1.0) with an increase in the Ti content. $Fe_{3-x}Ti_xO_4$ solid solution with the composition of $0.734 \leq x \leq 1.0$ proved the transformation to the tetragonal structure at pressures lower than the transition pressure to the orthorhombic phase (Fig. 1). We executed the single-crystal diffraction studies using DAC and SR facilities and elucidated electron deformation.

The present experiment aims to prove the Jahn-Teller transition of Fe_2TiO_4 from cubic-to-tetragonal structure at high pressures by electron-density distribution analysis using maximum entropy method (MEM) based on single-crystal diffraction intensities from SR. Furthermore the transition at low temperature below −110 °C has been also made for comparison with the transition at high pressure.

II. EXPERIMENT

The single-crystal sample of Fe_2TiO_4 ulvöspinel (x=1.0) was synthesized by floating zone (FZ) method. The chemical composition of the sample was analyzed by electron probe micro analyzer and the sample homogeneity was examined by secondary-emission image of scanning electron microscopy. Neither trace elements nor impurity was found in the samples.

Using SR at BL-10A in Photon Factory (KEK), Tsukuba, we performed high-pressure single-crystal structure analyses up to 12 GPa with a crump-type DAC with wide diffraction angle of 80° in 2θ, which is especially designed for the present experiment. Scintillation counter installed in the

TABLE I. Tetragonal spinels due to Jahn-Teller distortion N, I, and P indicate normal, inverse, and partially normal spinel structures, respectively. Jahn-Teller cations with (A) and (B) represent the cation position at the tetrahedral and octahedral sites.

Sample	Type		T_c (K)	T_N	a	c	c/a	Magnetism	Transition to	Reference
$MgMn_2O_4$	N	Mn^{3+}(B)			5.728	9.346	1.154			
$MnMn_2O_4$	N	Mn^{3+}(B)	1433		5.7621	9.4696	1.162		*Fd3m*	Muller and Roy (1974)
$FeMn_2O_4$	P	Mn^{3+}(B)			8.31	8.85	1.065			
$NiMn_2O_4$	N(P)	Mn^{3+}(B)	2303		8.382	8.382	1.000			Paladino (1953)
$NiMn_2O_4$	N(P)	Mn^{3+}(B)	1180						*Fd3m*	Gyorgyfalva (2003)
$CuMn_2O_4$	I(P)	Mn^{3+}(B) and Cu^{2+}(B)			5.971	8.964	1.062			
$ZnMn_2O_4$	N	Mn^{3+}(B)	21.3		5.720	9.245	1.143	Antiferro		Askrink *et al.* (1999)
$ZnMn_2O_4$	N	Mn^{3+}(B)	1323		5.720	9.245	1.143		*Fd3m*	Irani *et al.* (1962)
$LiMn_2O_4$	N	Mn^{3+}(B)	280		5.7960	8.2824	1.011			Yamada *et al.* (1995)
MgV_2O_4	I	V^{3+}(B)	60	60			0.993		$I4_1/amd$	
CdV_2O_4		V^{3+}(B)	97	35	6.170	8.619	0.998	Antiferro	$I4_1/amd$	Onoda *et al.* (2003)
ZnV_2O_4	N	V^{3+}(B)	51	40	5.9481	8.3753	0.996	Antiferro	$I4_1/amd$	Lee *et al.* (2004)
ZnV_2O_4	N	V^{3+}(B)						Antiferro	$I4_1/amd$	Ueda *et al.* (2003)

four-circle diffractometer was used for the detector, instead of charge coupled device or imaging plate detector because the measurements of the precise diffraction intensities and orientation matrix are significant for the calculation of maximum entropy method. Several intrinsic problems of DAC have been conquered using about 1.5 carat single-crystal diamond backing plates with (100) cut installed in the DAC.[15]

A mixture of ethanol, methanol, and water was applied as a pressure transmitting media, which guaranty hydrostaticity at pressures up to 12 GPa. The Fe_2TiO_4 single crystal of $60\times60\times20$ μm is placed in the gasket hole of 200 μm in diameter together with pressure marker of ruby chips and pressure transmitting media. A spring steel gasket was preindented to 60 μm in thickness. Pressure was measured by the ruby fluorescence method.[16]

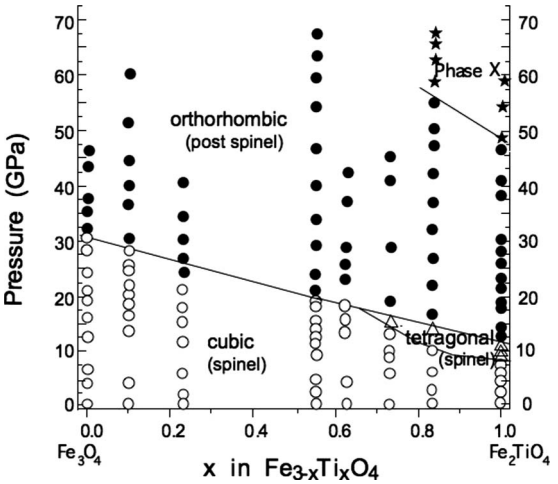

FIG. 1. Phase diagram of $Fe_{3-x}Ti_xO_4$ solid solution as a function of pressure. Phase boundary and transition pressure of $Fe_{3-x}Ti_xO_4$ spinel solid solutions were determined only from the experiments with increasing pressure. Back transformation to cubic spinel phase with decreasing pressure is hardly detected.

Intensive transmittance of SR for anvil or window in the x-ray path provides high signal-to-noise (S/N) ratio of the diffraction intensity, weak diffraction intensity, and sharp peak profiles. Since a small aperture angle of DAC gives a limited diffraction angle, the tunability of SR supplies an optimum and short wavelength, which has more advantage for accessing a large portion of reciprocal space, providing a large Q value $(=2\sin\theta/\lambda)^2$. We used a wavelength monochromated to $\lambda=0.61907$ Å ($E=20.0137$ keV) by Si (111) crystal monochromator. Four-circle diffractometer and scintillation counter were used for the present high-pressure diffraction study at BL-10A in KEK Tsukuba. Intensity measurement was carried out by stepping counts with fixing ϕ rotation. A narrow beam by the collimator of 80 μm in diameter was adopted because the gasket hole was 200 μm and the sample size was several ten microns cross. A receiving slit of 1° angle was used. The collimated beam through the evacuated guide pipe approached quite near to the DAC.

The intensity measurements of Fe_2TiO_4 at low temperatures up to −170 °C and ambient pressure were also executed using the laboratory x-ray source with 18 kW rotated-anode Mo $K\alpha$ radiation. The measurements using spherical single crystal of 130 μm have been performed by RIGAKU-AFC7R with nitrogen gas blow system. Temperature was measured by copper constantan thermocouple and the fluctuation of cooling temperature is 0.3–5 °C. All experimental conditions of the present diffraction studies are listed in Table II.

Powder-diffraction experiment has been also performed up to 60 GPa using a monochromated beam of synchrotron radiation at the undulator beam line BL-13A with wavelength about 30 KeV. A flat cassette-type imaging plate was used as a detector and the diffraction pattern of each sample was collected for 20–30 min with the collimated beam of 15–30 μm in diameter through the focusing mirrors. The powder-diffraction patterns with increasing pressure are shown in Fig. 2.

TABLE II. Diffraction intensity measurements under high-pressure condition.

	Cubic						Tetragonal			
Pressure (GPa)	0.0001	1.03	2.06	5.00	5.58	6.50	8.76	9.84	10.64	11.43
Diffractometer	AFC6S	AFC5R	AFC5R	AFC5R	AFC5R	AFC5R	PF	PF	PF	PF
Lattice constant										
a(Å)	8.5469(3)	8.5169(9)	8.4998(12)	8.4570(12)	8.4480(9)	8.4401(9)	8.4309(8)	5.9431	5.9350	5.9296
								(8.4048)	(8.3934)	(8.3857)
c(Å)								8.3567	8.3136	8.2836
c/a	1.0	1.0	1.0	1.0	1.0	1.0	1.0	0.9942	0.9905	0.9878
Cell volume (Å^3)	624.3	617.8	614.1	604.9	602.9	601.2	599.3	590.32	585.68	582.50
Data collection										
Wavelength (Å)	0.71069	0.71069	0.71069	0.71069	0.71069	0.71069	0.61907	0.61907	0.61907	0.61907
Beam size (μm)	500	100	100	100	100	100	100	100	100	100
2θ range	120	85.6	80.1	80.4	86.2	82.8				
Scan mode	2θ-ω	2θ-ω	2θ-ω	ω	ω	ω	ω	ω	ω	ω
	Bisec	ϕ fixed	ϕ fixed	ϕ fixed	ϕ fixed	ϕ fixed	ϕ fixed	ϕ fixed	ϕ fixed	ϕ fixed
Scan speed	2°/min	1°/min	1°/min	1°/min	0.01°/s	0.01°/s				
Gasket	Spring steel	Spring steel	Spring steel	Re	Re	Re	Re	Re	Re	Re
Pressure media	Meth-Eth	Meth-Eth	Meth-Eth	Meth-Eth	Meth-Eth	Meth-Eth	Meth-Eth	Meth-Eth	Meth-Eth	Meth-Eth
Culet size of DAC	500	500	400	400	400	400	400	400	400	400
Crystal size (mm)	120×100×80	130×90×50	80×60×40	80×60×40	80×60×40	80×60×40	60×40×40	60×40×40	60×40×40	60×40×40
No. of ref_{obs}	3242	368	472	546	528	370	570	634	756	606
No. of $ref_{independent}$	159	65	59	57	53	53	81	70	77	74
R(%)	1.69	3.41	4.45	4.28	4.44	4.60	3.40	3.60	4.08	3.86
wR(%)	2.03	2.16	2.92	2.57	1.91	1.76	2.65	2.77	4.27	4.13

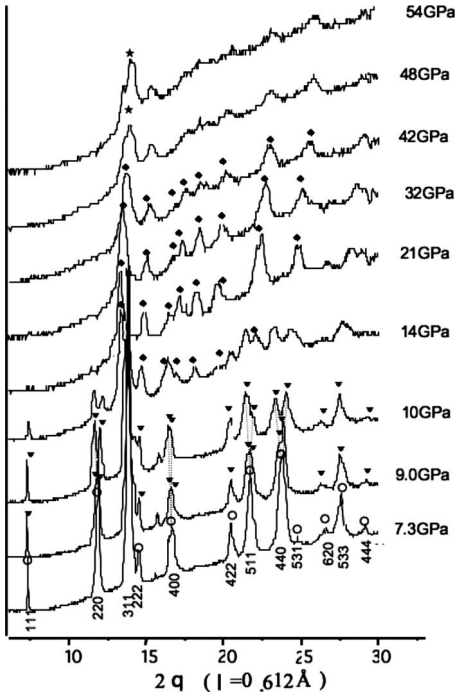

FIG. 2. Powder diffraction patterns of Fe_2TiO_4 with increasing pressure. Polymorphic phases are represented by symbol ○ for cubic spinel, ▼ for tetragonal spinel, ● for orthorhombic postspinel, and ★ for *X* phase.

III. STRUCTURE REFINEMENT

The electron-density distribution of Fe_2TiO_4 was investigated under high pressure at room temperature and low temperature under ambient pressure using MEM. Diffraction intensity measurements were conducted at high pressures of 1 atm, 1.03, 1.94, 2.06, 5.00, 5.58, 6.50, and 8.76 GPa for cubic phase and 9.64, 10.64, and 11.43 GPa for tetragonal. The measurements at low temperatures of 20, −50, and −100 °C for cubic phase and −110 and −170 °C for tetragonal phase have been conducted. First the conventional structure refinements have been undertaken by the full matrix least-squares program RADY.[17] Tetragonal and cubic structures of Fe_2TiO_4 have a space group, $I4_1/amd$ and $Fd3m$, respectively. Structure factor is calculated as

$$F_{cal}(\vec{h}) = K\sum_j a_j f_j(\vec{h}) \sum T_{js}(\vec{h})\exp\{2\pi i(hx_{js} + ky_{js} + lz_{js})\},$$

where K is a scale factor, $T(\boldsymbol{h})$ is temperature factor, and f_j indicates the atomic scattering factor of j atom. Fully ionized atomic scattering factor f_j was taken from *International Tables for X-Ray Crystallography, Vol. IV* (1974).[18] Anomalous dispersion parameters of $\Delta f'$ and $\Delta f''$ were taken into account in the atomic scattering factor of $f=f_0+\Delta f'+i\Delta f''$. The least-squares refinement is conducted by minimization of

$$\Delta = \sum_{\vec{h}} w(\vec{h})\{|F_{obs}(\vec{h})| - |F_{cal}(\vec{h})|\}^2.$$

Atomic coordinates, scale factor, anisotropic temperature factors, and isotropic extinction parameter were taken into account for the variable parameters. The converged structure parameters at each pressure and temperature are presented in Tables III and IV. The reliable factor (R) of the least-squares refinements was converged to $R=0.015–0.040$ at low temperatures and 0.03–0.09 at high pressures. The transition to the tetragonal phase takes place at about −110 °C at ambient pressure and the transition pressure is about 9.0 GPa.

IV. TEMPERATURE AND PRESSURE DEPENDENCE OF THE LATTICE CONSTANT

The cubic-to-tetragonal transition pressure was found at about 9 GPa and further tetragonal to orthorhombic at 12 GPa from powder-diffraction study. $Fe_{3-x}Ti_xO_4$ spinel solid solutions with less than $x=0.6$ do not transform to tetragonal but directly to orthorhombic $CaTi_2O_4$-type ($Cmcm$) structure.[9] The cubic lattice constant a considerably decreases up to 9 GPa in comparison with the thermal change at low temperatures. Then it splits to a and c of the tetragonal structure with $c/a<1$.

The transition to the low-temperature tetragonal phase takes place at about −110 °C. The lattice constant is lessened very slightly at temperatures from 20 to −110 °C (Fig. 3). The splitting to a and c is different from the case at high pressure and shows the ratio of $c/a>1$. The ratio of $c/a=1.0035(5)$ at −170 °C is a good agreement with $c/a=1.0050$ (Ishikawa and Syono, 1971).[2] These c/a ratios indicate that the tetragonal distortion at high pressures induced a slightly flatted lattice to the c axis. On the other hand, it brings an elongated structure at low temperature.

Volume of octahedron and tetrahedron with increasing pressure and with lowering temperature are continuously changed beyond the transition pressure and temperature, as shown in Fig. 4. The tetrahedral volume is more compressive in the both cases. The unit-cell volume is changed continuously in the cubic and tetragonal structures. The changes in the site volumes and unit-cell volumes prove the first-order transition with atomic displacement. The tetrahedral bond angel O-Fe-O, as shown in Fig. 5, is also an indicator of the tetragonal deformation. The cubic-to-tetragonal transition studied from thermodynamical aspects using Landau theory[19–21] can explain the transition mechanism due to the polyhedral strain and deformation of the phase transition.

V. MAXIMUM ENTROPY METHOD

MEM using x-ray single-crystal diffraction intensities clarifies electron deformation density due to electron configuration change under compression. The conventional difference Fourier synthesis of the structural studies at high pressures cannot provide accurate electron-density distribution because of the termination effect of the Fourier series, because DAC has a limited reciprocal space due to the small aperture angle. However, electron-density distribution analysis by MEM overcomes the difficulty and presents much more reliable electron distribution.

MEM is one method of the information processes and a statistical approach to satisfy the given information.[22] MEM was first applied for structure analysis.[23] MEM statistically

TABLE III. Structure refinement of Fe_2TiO_4 at high pressures. Calculated atomic coordinates, bond length, and site volume are presented.

	Cubic								Tetragonal		
Pressure (GPa)	0.0001	1.03	1.94	2.06	5.00	5.58	6.50	8.76	9.84	10.64	11.43
R(%)	1.69	3.30	4.12	4.54	4.28	4.23	4.63	3.40	3.60	3.99	3.86
wR(%)	2.03	1.47	2.92	2.92	2.57	1.76	1.75	2.65	2.77	3.06	4.13
A(Fe)	0 0 0									0 3/4 1/8	
B(Fe,Ti)	5/8 5/8 5/8									0 1/2 1/2	
Oxy x	0.3861(7)	0.3861(13)	0.3865(23)	0.3856(24)	0.3858(17)	0.3858(13)	0.3857(16)	0.3853(11)	0.0	0.0	0.0
y									0.0196(8)	0.0185(7)	0.0180(24)
z									0.2606(9)	0.2619(11)	0.2621(10)
$B_{eq}(A)$	0.868(1)	0.533(6)	0.631(10)	0.476(8)	0.564(5)	0.855(6)	0.620(10)	0.410(6)	0.404(23)	0.400(23)	0.296(37)
$B_{eq}(B)$	0.647(1)	0.361(9)	0.207(13)	0.297(10)	0.379(7)	0.518(8)	0.320(12)	0.192(8)	0.202(59)	0.265(56)	0.239(85)
B_{eq}(Oxy)	1.211(3)	1.012(15)	1.545(23)	0.991(18)	1.081(12)	1.092(13)	1.140(15)	0.766(8)	0.874(88)	0.559(79)	0.567(108)
Extinct (E-04)	8.34	2.92	5.93	3.97	3.07	2.89	3.08	4.52	1.157	0.893	0.385
A-O $\times 4$	2.0107(9)	2.0077(9)	2.0038(9)	2.0007(9)	1.9863(9)	1.9871(10)	1.9838(8)	1.9697(8)	1.9636(35)	1.9630(35)	1.9605(93)
B-O $\times 2$	2.0421(12)	2.0391(9)	2.0374(10)	2.0360(12)	2.0286(9)	2.0249(10)	2.0238(8)	2.0184(8)	2.0111(47)	1.9980(47)	1.9945(23)
$\times 4$	2.0421(12)	2.0391(9)	2.0374(10)	2.0360(12)	2.0286(9)	2.0249(10)	2.0238(8)	2.0184(8)	2.0206(23)	2.0240(23)	2.0252(78)
$\angle$O-A-O	109.47	109.47	109.47	109.47	109.47	109.47	109.47	109.47	109.60	109.97	110.04
$\angle$O-A-O	109.47	109.47	109.47	109.47	109.47	109.47	109.47	109.47	109.22	109.39	108.33
Vol(A)	4.172(1)	4.153(5)	4.123(5)	4.110(4)	4.022(5)	4.027(4)	4.006(4)	3.9922(4)	3.885(18)	3.881(18)	3.867(40)
Vol(B)	11.21(1)	11.16(1)	11.14(2)	11.12(1)	11.00(1)	10.94(1)	10.92(1)	10.85(1)	10.83(5)	10.80(5)	10.79(10)

TABLE IV. Structure refinement of Fe_2TiO_4 at low temperature.

	Cubic ($Fd3m$)			Tetragonal ($I4_1/amd$)	
Temperature (°C)	20	−50	−100	−150	−170
Lattice constant					
a(Å)	8.5297(3)	8.5226(10)	8.5205(20)	8.5035(23)*	8.4946(45)*
c(Å)	8.5297(3)	8.5226(10)	8.5205(20)	8.5237(30)	8.5247(34)
c/a	1.0	1.0	1.0	1.0024	1.0035
Cell volume (Å^3)	624.3	619.03	618.56	616.24	615.13
Data collection					
2θ range	120	80	92	92	80.4
Refinement					
No. of ref_{obs}	3242	410	516	535	390
No. of $ref_{independent}$	159	105	118	283	216
R(%)	1.69	2.12	2.20	2.24	1.60
wR(%)	2.03	1.91	1.98	2.08	1.27
A(Fe)		0 0 0		0 3/4 1/8	
B(Fe,Ti)		5/8 5/8 5/8		0 1/2 1/2	
Oxy x	0.3861(7)	0.3859(9)	0.3858(9)	0.0	0.0
y				0.0205(4)	0.0205(3)
z				0.2607(3)	0.2603(2)
$B_{eq}(A)$	0.868(1)	0.604(2)	0.620(2)	0.610(6)	0.569(5)
$B_{eq}(B)$	0.647(1)	0.413(2)	0.418(2)	0.436(24)	0.392(19)
B_{eq}(Oxy)	1.211(2)	1.015(4)	0.963(4)	1.026(56)	0.963(43)
Extinct (E-04)	8.34	39.30	45.55	0.453	0.586
Bond length					
A-O ×4 (Å)	2.0107(9)	2.0061(77)	2.0041(77)	1.9957(26)	1.9945(25)
B-O ×2 (Å)	2.0421(9)	2.0420(77)	2.0422(77)	2.0436(26)	2.0437(20)
×4 (Å)	2.0421(9)	2.0420(77)	2.0422(77)	2.0426(19)	2.0405(23)
∠O-A-O ×2	109.47	109.47	109.47	109.172	109.100
∠O-A-O ×4	109.47	109.47	109.47	109.621	109.657
Vol(A) (Å^3)	4.172(1)	4.143(4)	4.13(4)	4.08(1)	4.07(1)
Vol(B) (Å^3)	11.21(1)	11.21(13)	11.22(12)	11.24(4)	11.22(5)

estimates the most reliable electron-density distribution from the finite structure factors. Hence, the problem caused by the termination effect in the Fourier synthesis would be ignored. MEM was applied to the crystallographic problems by several experimental and theoretical approaches.[24–27] MEM was applied for single-crystal diffraction studies.[28–31]

The ideal entropy S in the MEM calculation is defined by

$$S = -\sum_{i}^{K} \rho'(\boldsymbol{r}_i) \ln \frac{\rho'(\boldsymbol{r}_i)}{\tau'(\boldsymbol{r}_i)}, \tag{1}$$

where the electron density $\rho'(\boldsymbol{r}_j)$ and the preliminary electron density $\tau'(\boldsymbol{r}_j)$ are represented by

$$\rho'(\mathbf{r}_i) = \frac{\rho(\mathbf{r}_i)}{\sum_i \rho(\mathbf{r}_i)} \quad \text{and} \quad \tau'(\mathbf{r}_i) = \frac{\tau(\mathbf{r}_i)}{\sum_i \tau(\mathbf{r}_i)}, \tag{2}$$

where $\tau'(\boldsymbol{r}_i)$ indicates an electron density one cycle before the iteration of the least-squares calculation of $\rho'(\boldsymbol{r}_i)$. Fourier transform of the estimated $\tau'(\boldsymbol{r}_i)$ provides $F_{cal}(\boldsymbol{h})$,

$$F_{cal}(\boldsymbol{h}) = V \sum_j \tau(\boldsymbol{r}_j) \exp(-2\pi i \boldsymbol{h} \cdot \boldsymbol{r}_j), \tag{3}$$

where V is the unit-cell volume. $\rho'(\boldsymbol{r}_i)$ is defined by

$$\rho(\boldsymbol{r}_i) = \tau(\boldsymbol{r}_i) \exp\left[\frac{\lambda F_{000}}{N} \sum_h \frac{w(\boldsymbol{h})}{\sigma^2(\boldsymbol{h})} \times \{F_{\mathrm{MEM}}(\boldsymbol{h}) - F_{obs}(\boldsymbol{h})\} \exp\{-2\pi i (\boldsymbol{h} \cdot \boldsymbol{r}_i)\} \right], \tag{4}$$

where N is the number of the observed structure factors $F_{obs}(\boldsymbol{h})$ and λ is a Lagrange undermined coefficient. F_{total} is a total number of electrons. Single-crystal diffraction study can directly measure many data of $F_{obs}(\boldsymbol{h})$ individually for all reflections. This is the reason why the MEM using single-crystal diffraction intensities can provide much more reliable results, compared with using powder diffraction. We applied

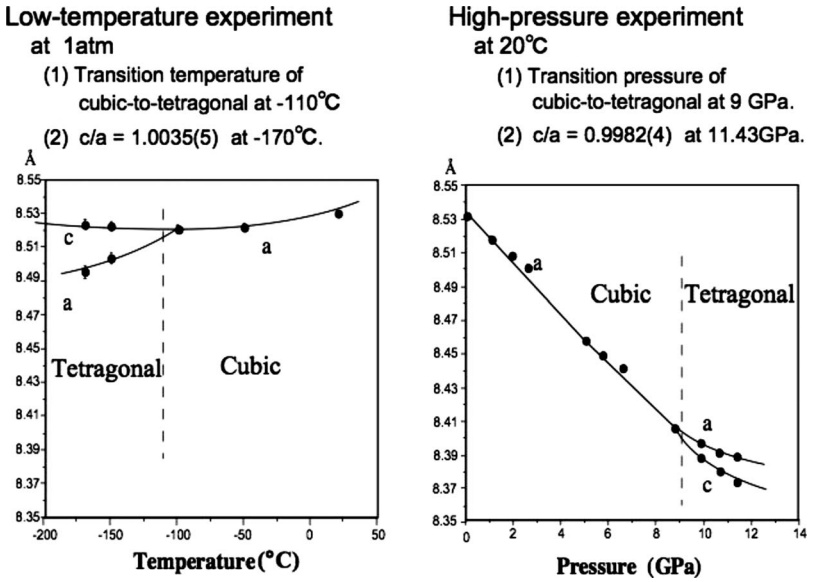

FIG. 3. Lattice constant as functions of temperature and pressure. Lattice constant of Fe_2TiO_4 under pressures was determined from 20 to 25 single-crystal reflections.

the method to clarify the anisotropy of electric conductivity of $FeTiO_3$ ilmenite under high-pressure condition[30] and pressure dependence of ferroelectricity of $KNbO_3$.[32]

VI. DIFFERENCE IN THE JAHN-TELLER EFFECT BETWEEN HIGH-PRESSURE AND LOW-TEMPERATURE CONDITIONS

A weak crystal-field stabilization energy (CFSE) effect by tetrahedral cations, $3d^1(Ti^{2+}, V^{4+})$, $3d^3(V^{2+}, Cr^{3+}, Mn^{4+})$, and $3d^6(Fe^{2+}, Co^{3+})$ introduce the cubic-to-tetragonal Jahn-Teller transition. High-spin state of the electron configuration interprets that the difference Fourier maps of Fe_2TiO_4 (Fig. 6) on to (100) at $y=0.25$ reveals a larger residual electron density of d_{z^2} than that of $d_{x^2-y^2}$ around the tetrahedral cation at −170 °C, indicating that the degeneracy of e orbit of for $^{IV}Fe^{2+}$ at the tetrahedral site is electronic state of d_{z^2} to $d_{x^2-y^2}$. The electronic state induces the tetragonal distortion with $c/a>1$. On the other hand the octahedral site is occupied by cations of $Ti^{4+}(3d^0)$ and $Fe^{2+}(3d^6)$ and the residual electron density around the octahedral cation in the map on to (001) can be explained by the d_{xy} orbit of Fe. Note that Ti^{4+} ideally has no d electron at the ground state.

Based on the high-spin state condition, degeneracy of e orbit at the tetrahedral site for Fe^{2+} prefers electronic state of the d_{z^2} orbit at low temperatures inducing the tetragonal distortion with $c/a>1$. But under high pressures $d_{x^2-y^2}$ is preferable and yields the distortion of $c/a<1$. MEM electron-density maps reveal the electron configuration of d_{z^2} state in the former and $d_{x^2-y^2}$ in the latter conditions, as shown in Fig. 7, which is on the plane parallel to (110) at $y=0.25$. The electronic spin distribution of d_{xy} orbit of $^{VI}Fe^{2+}$ at the octahedral site is more clearly disclosed in the tetragonal phase at high pressure in the MEM map on (001) at $z=0.5$ (Fig. 8) but the map at low temperature does not obviously show the d_{xy} distribution. The d_{xy} electron distribution at high pressure also induces the tetragonal phase with the flattened structure perpendicular to the c axis. But at low temperature the tetragonal phase slightly elongated to the c axis.

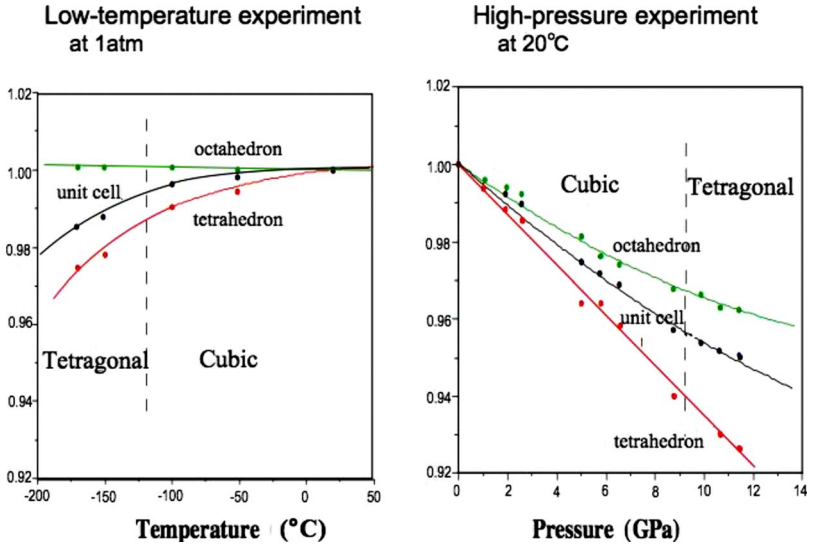

FIG. 4. (Color online) Unit cell, tetrahedral, and octahedral site volume changes with temperature and pressure.

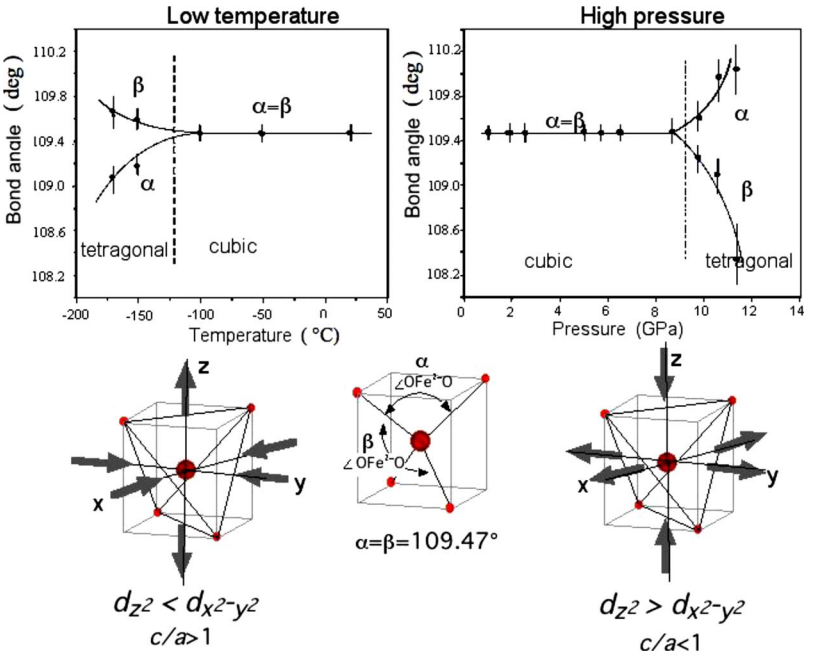

FIG. 5. (Color online) Bond angle O-Fe-O of the tetrahedron indicating the Jahn-Teller deformation. Tetrahedron in the tetragonal phase is compressed at high pressure and elongated at low temperature is elongated to the c axis. The bond angle is an indicator of the elongation and flattening of the unit cell with c/a. Deformation of the tetrahedron and the spin configuration in the tetragonal phase are proved.

The site symmetry of the tetrahedral site changes from $\bar{4}3m$ to $\bar{4}2m$ at the transition from the cubic to the tetragonal structure. The deformation to the tetragonal symmetry is visualized in Fig. 5 in which the arrows express the direction of the compression of tetrahedron. The tetragonal spin configurations in the both cases, high pressure and low temperature are presented together with the bond angle O-Fe-O and c/a in the figure.

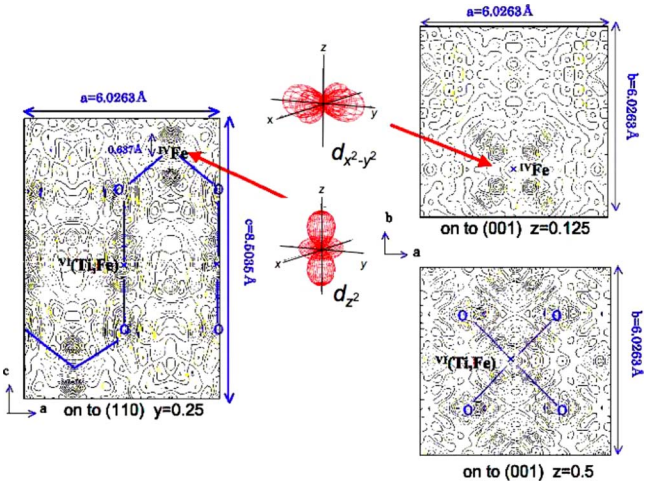

FIG. 6. (Color online) Difference Fourier map of Fe_2TiO_4 at −170 °C. The left map shows a section passing through the A site and parallel to (110). Contours are drawn at intervals of 0.2 $e/Å^{-3}$, starting from the 0.2 $e/Å^{-3}$ contour. Positive and negative contours are presented by solid and broken lines, respectively. The zero contour is omitted. Right maps present on the plane (001) at $z=0.125$ and 0.5. The former shows the residual electron around the tetrahedral cation Fe^{2+} atom and the latter that of the octahedral cation (Ti^{4+} and Fe^{2+}).

The CFSE by tetrahedral $Fe^{2+}(3d^6)$ introduces the cubic-to-tetragonal transition by the Jahn-Teller effect. The present experiment proves that Fe_2TiO_4 is a tetragonal structure with $c/a>1$ at low temperature and phonon-lattice interaction induces a cubic structure by thermal vibrational atoms and statistical atomic positional disorder at ambient conditions. Compression energy induces the splitting energy in the e-orbital electron configuration at high pressures and room temperature and brings a tetragonal structure with $c/a<1$.

VII. HIGH-PRESSURE SEQUENTIAL TRANSITION

Further high-pressure transition from the tetragonal-to-orthorhombic structure of Fe_2TiO_4 was found at 11 GPa. Rietveld profile fitting has been performed using program

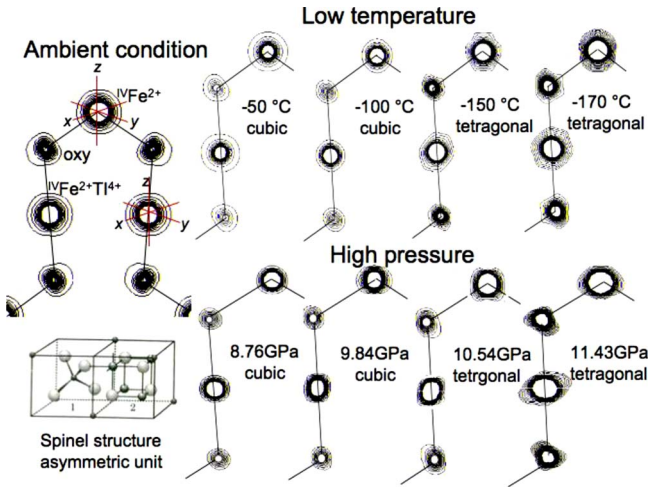

FIG. 7. (Color online) Electron-density distribution by MEM on the section of (110). All maps are drawn with the contour interval of 0.02 $e/Å^{-3}$, starting from the 0.02 $e/Å^{-3}$ contour.

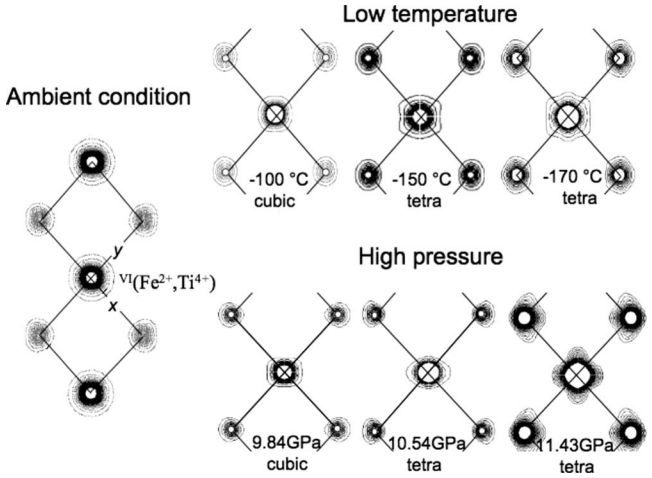

FIG. 8. Electron-density distribution by MEM of the section of (001) at $z=0.5$. The contour interval is same in Fig. 5.

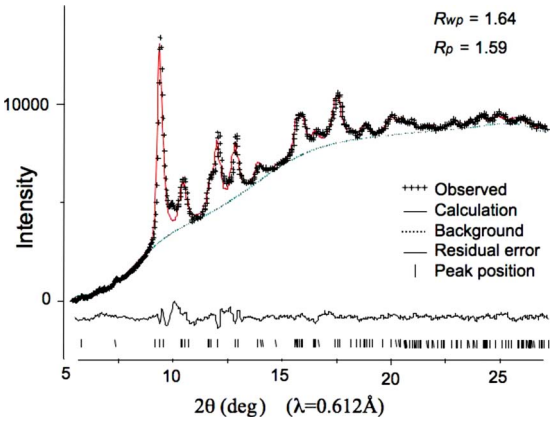

FIG. 9. (Color online) Rietveld profile fitting of orthorhombic phase using powder-diffraction pattern taken at 27 GPa. The observed data (dotted line) and Rietveld refinement (solid line) are presented. The residual peaks of I_{obs}-I_{cal} are presented in the lower level. The bars represent the peak positions of the orthorhombic phase.

RIETAN.[33] Three possible structures of $CaMn_2O_4$,[34] $CaTi_2O_4$,[35] and $CaFe_2O_4$ (Refs. 33 and 36) were applied as the initial structure model. The following refinement parameters are taken into account in the Rietveld analysis of the orthorhombic phase at 27 GPa: scale factor, background, lattice constant, atomic position, site occupancy, profile parameter, and asymmetric parameter. The structure model providing the best reliable factor is the $CaTi_2O_4$ type model [*Cmcm* $z=4$, $a=2.7876(8)$ Å, $b=9.463(3)$ Å, and $c=9.421(2)$ Å]. The final reliable parameters are $R_P=1.59$ and $wR_P=1.64$ and all converged structure parameters are listed in Table V.

Two cation sites, $M1(4c)$ and $M2(8f)$, are sixfold coordination sites. The structure is composed of a herringbone octahedra array (Figs. 9 and 10). One of Fe^{2+} occupies the $M1$ site and the other Fe^2 is disorderly located at the $M2$ site with Ti^{4+} ion. From the present powder diffraction, the cation ordering of Ti^{4+} and Fe^{2+} in the $M2$ site could not be detected. The cation distribution in the high-pressure phases probably reflects the octahedral site of the inverse spinel structure of Fe_2TiO_4.

TABLE V. Result of the Rietveld analysis of high-pressure phase of Fe_2TiO_4. Powder diffraction pattern of Fe_2TiO_4 at 27 GPa was used for the Rietveld profile fitting analysis. Space group *Cmcm* (No.63) $z=4$. Lattice constant $a=2.7876(8)$, $b=9.463(3)$, and $c=9.421(2)$.

Atom	Wyck.	Site sym.	Multiplicity	Occupancy	x	y	z
Fel	4*c*	2 mm	0.25	1.0	0.0	0.3809(8)	0.25
Til	8*f*	..m	0.50	0.5	0.0	0.1331(7)	0.0753(6)
Fe2				0.5			
O1	4*b*	..2/m	0.25	1.0	0.0	0.0581(7)	0.0.25
O2	4*c*	2mmj	0.25	1.0	0.0	0.2421(10)	0.6028(7)
O3	8*f*	..m	0.5	1.0	0.0	0.5	0.0

Profile fitting parameters

Scale factor	S	$2.37(1)\times 10$
Full width at half maximum parameter	U	3.650(2)
	V	$7.90(2)\times 10^{-2}$
	W	$2.502(2)\times 10^{-2}$
Asymmetry parameter	A_0	0.70(1)
	A_1	$-2.1(1)\times 10^{-3}$
	A_2	$9.7(8)\times 10^{-4}$
Extinction parameter	h_{Lo}	0.66(3)
	h_{L1}	0.6(1)
	h_{H0}	0.87(2)
	h_{H1}	−1.0(1)

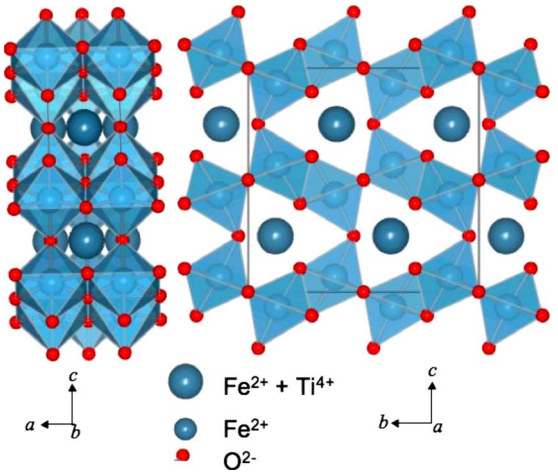

FIG. 10. (Color online) Structure of orthorhombic Fe_2TiO_4 [*Cmcm* $z=4$, $a=2.7876(8)$ Å, $b=9.463(3)$ Å and $c=9.421(2)$ Å]. The orthorhombic structure of Fe_2TiO_4 is an isostructure of $CaTi_2O_4$.

In addition, another higher-pressure polymorph was found above 45 GPa (Fig. 2). This phase is reversibly changed to the orthorhombic phase with reducing pressure. The new structure cannot be analyzed because only one new obvious reflection was observed.

VIII. BULK MODULUS OF THE $Fe_{3-x}Ti_xO_4$ SPINEL SOLID SOLUTIONS

Bulk modulus of the spinel phase by the second-order Birch-Murnaghan equation is calculated from the pressure dependence of the unit-cell volumes determined by Rietveld profile fitting of all powder-diffraction data, the number of observed data is limited to only five data. Then those data fitted to the first-order BM are $K_0=238.1(4.2)$ GPa and $K'=7.6(2.4)$. When K' is fixed to $K'=4.0$, $K_0=250.8(2.5)$ GPa. The bulk modulus of Fe_2TiO_4 spinel is much larger than that of Fe_3O_4. The bulk modulus of Fe_3O_4 is $K_0=183.4(8.1)$ GPa and $K_0'=7.1(2.9)$.

ACKNOWLEDGMENTS

The present investigation was performed under the auspices of KEK Proposal No. 2004G229 for powder-diffraction study at BL-13A and BL-18C. The authors would like to express their thanks to F. Takei at Osaka University for providing the single crystal of Fe_2TiO_4 grown by FZ method.

[1] T. Yamanaka, A. Uchida, and Y. Nakamoto, Am. Mineral. **93**, 1874 (2008).
[2] Y. Ishikawa and Y. Syono, Phys. Rev. Lett. **26**, 1335 (1971).
[3] H. N. Oak, K. S. Baek, and S. J. Kim, Phys. Status Solidi B **208**, 249 (1999).
[4] K. J. Kim, J. H. Lee, and S. H. Lee, J. Magn. Magn. Mater. **279**, 173 (2004).
[5] M. Isobe and Y. Ueda, J. Phys. Soc. Jpn. **71**, 1848 (2002).
[6] S. Senz, W. Blum, and D. Hesse, Philos. Mag. A **81**, 109 (2001).
[7] W. A. Dollase and H. S. C. O'Neill, Acta Crystallogr., Sect. C: Cryst. Struct. Commun. **53**, 657 (1997).
[8] S. Akimoto, T. Katsura, and M. Yosida, J. Geomagn. Geoelectr. **9**, 165 (1957).
[9] L. Neel, Adv. Phys. **4**, 191 (1955).
[10] R. Chevallier, J. Bolfa, and S. Mathieu, Bull. Soc. Fr. Mineral. Cristallogr. **78**, 307 (1955).
[11] W. O'Reilly and S. K. Banerjee, Phys. Lett. **17**, 237 (1965).
[12] Z. Kakol, J. Sabol, and J. M. Honig, Phys. Rev. B **43**, 649 (1991).
[13] B. A. Wechsler, D. H. Lindsley, and C. T. Prewitt, Am. Mineral. **69**, 754 (1984).
[14] H. H. Hamdeh, K. Barghout, J. C. Ho, P. M. Shand, and L. L. Miller, J. Magn. Magn. Mater. **191**, 72 (1999).
[15] T. Yamanaka, T. Fukuda, T. Hattori, and H. Sumiya, Rev. Sci. Instrum. **72**, 1458 (2001).
[16] G. J. Piermarini, S. Block, J. D. Barnett, and R. A. Forman, J. Appl. Phys. **46**, 2774 (1975).
[17] S. Sasaki and K. Tsukimura, J. Phys. Soc. Jpn. **56**, 437 (1987).
[18] T. Hahn, *International Tables for X-Ray Crystallography* (Kyonoch Press, Birmingham, England, 1974).
[19] J. D. Axe and Y. Yamada, Phys. Rev. B **24**, 2567 (1981).
[20] S. A. Hayward and E. K. H. Salje, Phase Transitions **68**, 501 (1999).
[21] M. A. Carpenter, A. I. Becerro, and F. Seifert, Am. Mineral. **86**, 348 (2001).
[22] E. T. Jaynes, IEEE Trans. Syst. Sci. Cybern. **4**, 227 (1968).
[23] D. M. Collins, Nature (London) **298**, 49 (1982).
[24] R. Narayan and R. Nityananda, Acta Crystallogr., Sect. A: Cryst. Phys., Diffr., Theor. Gen. Crystallogr. **38**, 122 (1982).
[25] S. W. Wilkins, J. N. Varghese, and M. S. Lehmann, Acta Crystallogr., Sect. A: Found. Crystallogr. **39**, 47 (1983).
[26] A. K. Livesey and J. Skilling, Acta Crystallogr., Sect. A: Found. Crystallogr. **41**, 113 (1985).
[27] J. Navaza, Acta Crystallogr. A **42**, 212 (1986).
[28] K. Yamamoto, Y. Takahashi, K. Ohshima, F. Okamura, and K. Yukino, Acta Crystallogr., Sect. A: Found. Crystallogr. **52**, 606 (1996).
[29] M. Merli, A. Pavese, and M. Ranzini, Phys. Chem. Miner. **29**, 455 (2002).
[30] S. Israel, R. Saravanan, N. Srinivasan, and S. K. Mohanlal, J. Phys. Chem. Solids **64**, 879 (2003).
[31] T. Yamanaka, Y. Komatsu, and H. Nomori, Phys. Chem. Miner. **34**, 307 (2007).
[32] T. Yamanaka, T. Okada, and Y. Nakamoto, Phys. Rev. B **80**, 094108 (2009).
[33] F. Izumi and T. Ikeda, Mater. Sci. Forum **321-324**, 198 (2000).
[34] H. G. Giesber, W. T. Pennington, and J. W. Kolis, Acta Crystallogr., Sect. C: Cryst. Struct. Commun. **57**, 329 (2001).
[35] M. P. Rogge, J. H. Caldwell, D. R. Ingram, C. E. Green, M. J. Geselbracht, and T. Siegrist, J. Solid State Chem. **141**, 338 (1998).
[36] B. F. Decker and J. S. Kasper, Acta Crystallogr. **10**, 332 (1957).